CHAPTER 4

SCATTERING OF A MPS PULSE FROM COMPRESSIBLE AND RIGID SPHERES

4.1 Introduction

The need to study and understand acoustic and electromagnetic scattering arises in diverse areas, such as optics, plasma physics, geophysics, antennas and remote sensing. A significant amount of work has been done on scattering of short Gaussian pulses using integral equation methods, e.g., MFIE, and EFIE [150,151], both in the frequency and time domain. Time-domain analysis can be effected by FDTD techniques [150]. Excellent agreement between the results obtained by these methods and those based on the classical Mie series [152] has been achieved. Scattered and internal fields due to a polarized Gaussian beam incident on a dielectric sphere have been discussed in the optical range [155] using the T-matrix approach. In this analysis the beam is represented as an angular spectrum of plane waves.

In this chapter we study the acoustic scattering of the modified power spectrum (MPS) [27] pulse from rigid and compressible spheres. The advantage of using a MPS pulse over quasi-monochromatic Gaussian beams or pulsed plane waves is its superior focusing properties, which in turn are due to its localization in space and time. This trait makes such a pulse important for remote sensing purposes. Our procedure for obtaining scattered spectra can be outlined as follows:

1. Obtain the scattered field of a plane wave incident on a sphere;
2. Multiply the scattered field obtained in step (1) by the spectrum of a focus wave mode (FWM) pulse and integrate over the spatial spectral components;

3. Multiply the result of step (2) by an appropriate weighting function $F(\beta)$ and integrate over the parameter β to obtain the MPS pulse scattered field.

Our work extends research in this area undertaken by Power *et al.* [73] previously.

4.2 Source Free Focus Wave Mode Solution

Consider the 3-D scalar wave equation

$$(\nabla^2 - \frac{1}{c^2}\frac{\partial^2}{\partial t^2})\psi(\mathbf{r},t) = 0. \tag{4.2.1}$$

An azimuthally symmetric solution to Eq. (4.2.1) can be expressed as a Fourier-Hankel superposition, viz.,

$$\Psi(\rho,z,t) = \frac{1}{2\pi}\int_0^\infty d\chi \int_{-\infty}^{\infty} dk_z \int_{-\infty}^{\infty} d\omega \psi\tilde{\Psi}(\chi,k_z,\omega)\chi J_0(\chi\rho)e^{-ik_z z}e^{i\omega t}. \tag{4.2.2}$$

Introducing (4.2.2) into (4.2.1) results in the constraint

$$\frac{1}{2\pi}\int_0^\infty d\chi \int_{-\infty}^{\infty} dk_z \int_{-\infty}^{\infty} d\omega\left[\chi^2 + k_z{}^2 - (\omega/c)^2\right]\tilde{\Psi}(\chi,k_z,\omega)\chi J_0(\chi\rho)e^{-ik_z z}e^{i\omega t} = 0, \tag{4.2.3}$$

which implies that

$$\left[\chi^2 + k_z{}^2 - (\omega/c)^2\right]\tilde{\Psi}(\chi,k_z,\omega) = 0. \tag{4.2.4}$$

In order to have a nonzero spatio-temporal spectrum $\tilde{\Psi}(\chi,k_z,\omega)$ and, as a consequence, to obtain nontrivial solutions $\Psi(\rho,z,t)$ to the source-free homogenous scalar wave equation (4.2.1), it follows that the dispersion relation

$$\left[\chi^2 + {k_z}^2 - (\omega/c)^2\right] = 0\,, \tag{4.2.5}$$

must hold for all $\chi \in [0,\infty)$ and $k_z, \omega \in (-\infty,\infty)$. A specific spectrum that satisfies (4.2.4) is given by [43]

$$\tilde{\Psi}_\beta(\chi, k_z, \omega) = \frac{\pi^2}{i\beta}\, e^{-\chi^2 a_1/4\beta}\, \delta\left[k_z - \left(\chi^2/4\beta - \beta\right)\right]\delta\left[\omega/c - \left(\beta + \chi^2/4\beta\right)\right]. \tag{4.2.6}$$

The resulting wave solution is the FWM pulse [cf., also, Chapter 2]

$$\Psi_\beta(\rho, z, t) = e^{i\beta(z+ct)}\, \frac{e^{-\beta\rho^2/\left[a_1 + i(z-ct)\right]}}{4\pi i\left[a_1 + i(z-ct)\right]}\,. \tag{4.2.7}$$

For large values of βa_1, the FWM behaves as a plane wave moving in the negative z direction. On the other hand, for values $\beta a_1 << 1$, it behaves as a highly localized wavepacket moving predominantly in the positive z direction.

4.3 The Incident Pulse on the Sphere

The MPS pulse was suggested by Ziolkowski [27] as a finite energy LW solution to the homogeneous scalar wave equation. In the following we will use the MPS pulse given in Eq. (2.4.1.4) with $a_2 = q = 1$, viz.,

$$\Psi_{MPS}(\rho, z, t) = \frac{1}{\left(a_1 + i(z-ct)\right)\left((s/p) + 1\right)}\, e^{-bs/p}, \tag{4.3.1a}$$

where

$$s = \frac{\rho^2}{\left(a_1 + i(z-ct)\right)} - i(z+ct)\,,\ \rho = \sqrt{x^2 + y^2}\,, \tag{4.3.1b}$$

and a_1, b and P are free parameters. This pulse was used by Power *et al*. [73] to investigate the backscattering from metallic spheres. In this chapter, we shall extend their work by determining the bistatic scattering from soft and hard spheres. In our numerical work, we shall use the same MPS pulse parameters, viz., $a_1 = 4\times10^{-3}\text{m}$, $b = 750\ \text{m}^{-1}$ and $p = 300$, used in Ref. [73]. For these parameters, the waist of the pulse is 4.0 cm and the upper limit of the temporal spectrum is restricted to $\omega_{\max} = \left(c/a_1\right) = 2\pi f_{\max}$, i.e., $f_{\max} = 59.6$ KHz.

4.4 Bistatic Scattered Fields Arising from a Plane Wave Incident on a Compressible Sphere

A plane wave incident in the direction θ,ϕ can be represented by

$$\Phi_{inc} = e^{i\mathbf{k}.\mathbf{r}} = e^{ikr\cos\gamma}, \tag{4.4.1a}$$

where γ is the angle between the position vector $\mathbf{r} \equiv \left(r,\theta_0,\phi_0\right)$ and the wave vector $\mathbf{k} \equiv \left(k,\theta,\phi\right)$. The time dependence factor $e^{-i\omega t}$ is suppressed for simplicity, and in what follows we use the standard relationship

$$\cos\gamma = \cos\theta_0\cos\theta + \sin\theta_0\sin\theta\cos\left(\phi-\phi_0\right). \tag{4.4.1b}$$

This plane wave can be expanded in terms of Legendre polynomials and spherical Bessel functions as

$$e^{ikr\cos\gamma} = \sum_{n=0}^{\infty}(2n+1)i^n P_n\left(\cos\gamma\right) j_n(kr). \tag{4.4.1c}$$

Using the addition theorem given by Eq. (8.814) in Ref. [144], we obtain

$$P_n(\cos\gamma) = \sum_{m=0}^{n} \varepsilon_m \frac{(n-m)!}{(n+m)!} P_n^m(\cos\theta) P_n^m(\cos\theta_0) \cos\left(m(\phi - \phi_0)\right), \tag{4.4.2a}$$

where P_n, P_n^m are Legendre polynomial and associated functions, respectively, and

$$\varepsilon_m = \begin{cases} 1 & m = 0 \\ 2 & m \neq 0 \end{cases}. \tag{4.4.2b}$$

The scattering of a plane wave from a sphere has been discussed in many texts [138,148,149]. The scattered field can be conceived as a series of concentric spherical waves diverging from the scatterer. Consequently, it can be represented mathematically by the following form:

$$\Phi_{SCP} = \sum_{n=0}^{\infty} A_n P_n(\cos\gamma) h_n^{(2)}(kr). \tag{4.4.3}$$

Here, $h_n^{(2)}(kr)$ is the spherical Hankel function of second kind of order n and A_n is a coefficient determined from the boundary conditions. The subscript SCP stands for the scattered field due to an incident plane wave. For the case of a soft sphere of radius a, we have

$$A_n = -(i)^n (2n+1) \left[\frac{j_n'(ka) + i\alpha_n j_n(ka)}{h_n^{(2)'}(ka) + i\alpha_n h_n^{(2)}(ka)} \right] \tag{4.4.4}$$

and, as a result, the scattered field is given by

$$\Phi_{SCP} = -\sum_{n=0}^{n=\infty} (i)^n (2n+1) \left[\frac{j_n'(ka) + i\alpha_n j_n(ka)}{h_n^{(2)'}(ka) + i\alpha_n h_n^{(2)}(ka)} \right] P_n(\cos\gamma) h_n^{(2)}(kr). \tag{4.4.5}$$

From the expansion of $\cos\gamma$, given in Eq. (4.4.1c), and Eq. (4.4.5), it follows that the scattered field from a soft sphere at any observing point along the negative z-axis $\left(\theta_0 = \pi\right)$ due to an incident plane wave $(\theta,0)$ assumes the form

$$\Phi_{SCP} = -\sum_{n=0}^{n=\infty} (-i)^n (2n+1)\left[\frac{j_n'(ka) + i\alpha_n j_n(ka)}{h_n^{(2)'}(ka) + i\alpha_n h_n^{(2)}(ka)}\right] P_n(\cos\theta) h_n^{(2)}(kr)\,. \tag{4.4.6a}$$

Next, the well known backscattered field $(\theta = 0)$ is given by

$$\Phi_{BSCP} = -\sum_{n=0}^{n=\infty} (-i)^n (2n+1)\left[\frac{j_n'(ka) + i\alpha_n j_n(ka)}{h_n^{(2)'}(ka) + i\alpha_n h_n^{(2)}(ka)}\right] h_n^{(2)}(kr)\,, \tag{4.4.6b}$$

where

$$\alpha_n = \frac{i\rho c}{\rho_e c_e}\left[\frac{j_n'(k_e a)}{j_n(k_e a)}\right], \tag{4.4.7}$$

and

ρ is the density of the infinite medium surrounding the sphere;

c is the velocity of the infinite medium surrounding the sphere;

c_e is the speed of the wave propagation in the sphere;

ρ_e is the density of the material of the sphere;

a is the radius of the sphere;

BSCP denotes the backscattered field of the plane waves;

κ, κ_e are the compressibilities of the surrounding medium and the material of the sphere, respectively.

In addition, $k_e = \left(\omega/c_e\right)$, $k = \left(\omega/c\right)$, $c = \left(1/\sqrt{\rho\kappa}\right)$ and $c_e = \left(1/\sqrt{\rho_e \kappa_e}\right)$. The prime superscript in Eq. (4.4.6) signifies differentiation with respect to the argument. The medium outside the sphere is isotropic and homogeneous.

4.5 Bistatic Scattering of a Source-Free FWM from a Soft Sphere

In order to determine the scattered field produced by the interaction of a source-free FWM with a sphere, we multiply the FWM spectrum, given in Eq. (4.2.6), with the plane wave scattered field, given in Eq. (4.4.3), and integrate over the spatial spectral components, viz.,

$$\Psi_{SCF}(r,\theta_0,\phi_0,\omega) = \frac{1}{(2\pi)^3}\int_{R^3} d\mathbf{k}\,\tilde{\Psi}_\beta(\mathbf{k},\omega)\,\Phi_{SCP}(r,\theta,\theta_0,\phi,\phi_0,\omega), \tag{4.5.1}$$

or, more specifically,

$$\begin{aligned}\Psi_{SCF}\left(r,\theta_0,\phi_0,\omega\right) = \int_0^{2\pi} d\phi \int_{-\infty}^{\infty} dk_z \int_0^{\infty} d\chi\chi \frac{\pi^2}{i\beta} e^{-\chi^2/4\beta}\delta\left(k_z - \left(\left(\chi^2/4\beta\right)-\beta\right)\right) \\ \times \delta\left(\omega/c - \left(\left(\chi^2/4\beta\right)+\beta\right)\right)\sum_{n=0}^{\infty} A_n h_n^{(2)}(kr)\,P_n\left(\cos\gamma\right),\end{aligned} \tag{4.5.2}$$

with the subscript SCF standing for the scattered field due to the incident FWM. It should be noted that $k = \sqrt{k_z^2 + \chi^2}$ and $\cos\theta = k_z/k$. We use, next, the identity

$$\delta\left(\omega/c - \left(\left(\chi^2/4\beta\right)+\beta\right)\right) = \frac{\sqrt{\beta}}{c\sqrt{\left(\omega/c\right)-\beta}}\delta\left(\chi - \sqrt{4\beta\left(\omega/c-\beta\right)}\right)u\left(\omega/c-\beta\right). \tag{4.5.3}$$

The step function ensures that the value of the parameter β is less than ω/c. Next, we insert Eq. (4.5.3) into Eq. (4.5.2) and perform the integrations over the variables k_z, χ and ϕ following a procedure analogous to that used by Power *et al*. [73]. The integration over ϕ equals zero for all m values [cf. Eq. (4.4.2)] except $m = 0$. Assuming, for simplicity, that the observation point lies on the $x-z$ plane ($\phi_0 = 0$), we obtain

$$\psi_{SCF}\left(r,\theta_0,\omega\right) = \frac{u\left(\omega/c-\beta\right)}{2ic} e^{-a_1(\omega/c-\beta)}\sum_{n=0}^{\infty} A_n h_n^2\left(\omega r/c\right)P_n\left(\frac{2\beta c}{\omega}-1\right)P_n\left(\cos\theta_0\right). \tag{4.5.4}$$

The constraint $(\omega/c) > \beta$ ensures the effective decay of the exponential factor and, hence, the existence of the scattered field.

4.6 Scattering of a MPS Pulse from a Compressible Sphere

The finite energy MPS pulse [cf. Eq. (4.3.1)] was originally derived by Ziolkowski [27] as a superposition of infinite energy FWMs; specifically,

$$\Psi_{MPS}(\mathbf{r},t) = \int_0^\infty d\beta F(\beta)\Psi_{FWM}(\mathbf{r},t;\beta), \tag{4.6.1}$$

where the weighting function $F(\beta)$ is given by

$$F(\beta) = \begin{cases} 4\pi i p e^{-(\beta p - b)} & \beta \geq b/p \\ 0 & 0 \leq \beta \leq b/p \end{cases} \tag{4.6.2}$$

As a consequence, the scattered field due to an incident MPS pulse can be found by multiplying the FWM scattered field [cf. Eq. (4.5.4)] by the weighting function $F(\beta)$ and integrating over β. On the observation plane $\phi_0 = 0$, we have

$$\begin{aligned} \psi_{SCMC}(r,\theta_0,\omega) &= \int_0^\infty d\beta\, F(\beta)\, \psi_{SCF}(r,\theta_0,\beta,\omega) \\ &= \int_{b/p}^{\omega/c} d\beta \frac{2\pi p}{c} e^{-a_1(\omega/c-\beta)} \sum_{n=0}^{\infty} A_n h_n^{(2)}(kr)\Big|_{k=\omega/c} e^{-(\beta p - b)} P_n(\cos\theta_0) P_n\left(\frac{2\beta c}{\omega} - 1\right). \end{aligned} \tag{4.6.3}$$

We introduce, next, the change of variable $\zeta = (2\beta c/\omega) - 1$ and integrate by parts [cf., also, Ref. [73]]. This results in the scattered field

$$\Psi_{SCMC}(r,\theta_0,\omega) = \frac{\pi p\omega}{c^2}\sum_{n=0}^{\infty} A_n\Big|_{k=\omega/c}\, h_n^{(2)}(\omega r/c)P_n(\cos\theta_0)$$
$$\times\left[e^{-a_1(\omega/c-b/p)}\left(\frac{P_n(\zeta_0)}{\sigma}+\frac{P_n'(\zeta_0)}{\sigma^2}+\ldots+\frac{P_n^n(\zeta_0)}{\sigma^{n+1}}\right)\right.$$
$$\left.-e^{(-\omega p/c+b)}\left(\frac{P_n(1)}{\sigma}+\frac{P_n'(1)}{\sigma^2}+\ldots+\frac{P_n^n(1)}{\sigma^{n+1}}\right)\right], \qquad (4.6.4)$$

where

$$\sigma = \frac{\omega}{2c}\left(p-a_1\right), \quad \zeta_0 = \frac{2bc}{p\omega}-1. \qquad (4.6.5)$$

The scattering of a MPS pulse propagating along the z-axis from a sphere located at the origin can be envisioned as the superposition of the scattering of a set of plane waves with different amplitudes and spectral angles θ. This is depicted in Fig. 4.1.

In our computations we choose $/c$ in the range 1 to $1000\ \mathrm{m}^{-1}$. This will give large values for σ

evaluating the absolute value of the spectrum. However, for the sake of higher accuracy, especially for lower values of ω/c

numerical calculations.

4.7 Scattering of a MPS Pulse from a Rigid Sphere

equivalently as α_n [cf. Eq. (4.4.7)] approaches zero, the impedance of the sphere

$$\Phi_{SCPR} = \sum_{n=0}^{n=\infty} -(i)^n(2n+1)\left[\frac{j_n'(ka)}{h_n^{(2)'}(ka)}\right]P_n(\cos\gamma)h_n^{(2)}(kr). \qquad (4.7.1)$$

Similarly to Eq. (4.4.6), the scattered pressure field at any point along the negative z-axis $\left(\theta_0 = \quad\right)$ from the rigid sphere due to an incident plane wave in the x-z plane with an arbitrary angle θ can be obtained with the replacement of $P_n(\cos\quad)$ and $(i)^n$ by $P_n(\cos\theta)$ and $(-i)^n$. If $\theta = 0$, the backscattered field becomes

$$\Phi_{BSCPR} = \sum_{n=0}^{n=\infty} -(-i)^n(2n+1)\left[\frac{j_n'(ka)}{h_n^{(2)'}(ka)}\right]h_n^{(2)}(kr), \tag{4.7.2}$$

where the relationships $P_n(-1) = (-1)^n$ and $P_n(1) = 1$ have been used.

Following a procedure analogous to that used in the previous section, we find that the general (bistatic) scattered field due to an incident MPS pulse on a rigid sphere assumes the form

$$\begin{aligned}\psi_{SCMR}(r,\theta_0,\omega) = \frac{\pi p\omega}{c^2}\sum_{n=0}^{\infty}\left[\frac{j_n(ka)}{h_n^{(2)}(ka)}\right]'\Bigg|_{k=\omega/c} & h_n^{(2)}(\omega r/c)P_n(\cos\theta_0) \\ \times\Bigg[e^{-a_1(\omega/c-b/p)}&\left(\frac{P_n(\zeta_0)}{\sigma}+\frac{P_n'(\zeta_0)}{\sigma^2}+\ldots+\frac{P_n^n(\zeta_0)}{\sigma^{n+1}}\right) \\ -e^{(-\omega p/c+b)}&\left(\frac{P_n(1)}{\sigma}+\frac{P_n'(1)}{\sigma^2}+\ldots+\frac{P_n^n(1)}{\sigma^{n+1}}\right)\Bigg],\end{aligned} \tag{4.7.3}$$

where the subscript SCMR stands for the scattering of a MPS pulse from a rigid sphere.

4.8 Numerical Results

A comparison of the time history of the reconstructed incident MPS pulse, based on a discrete form of Huygens' principle [153] with N (number of annular sections) = 30, $\Delta\rho$ (transverse spacing) = 4 mm and a = 116 mm, and that of the exact one is depicted in Fig.

4.2. A slight difference between the amplitudes of the frequency content of these two pulses due to the discretization at the source plane is shown in Fig. 4.3.

We have investigated the difference between the backscattered spectrum of a compressible and that of a rigid sphere using Eqs. (4.6.4) and (4.7.3), respectively, with ambient medium parameters $c = 1500\ \mathrm{m/s}$ and $\rho = 10^3\ \mathrm{kg/m^3}$. The effect of varying the speed c_e on the backscattered spectrum is shown in Fig. 4.4 for a spherical scatterer of radius $a = 3\ \mathrm{cm}$, density $\rho_e = 7.8\times 10^3\ \mathrm{kg/m^3}$ and speeds $c_e = (1.5,\ 3,\ 4.5)\times 10^3\ \mathrm{m/s}$. It is seen that as the speed c_e increases, the spacing between the spectral dips increases. Figure 4.5 shows the variation of the spectrum with the radius of a soft sphere. The spacing between adjacent dips shortens as the radius increases. To focus on this spacing, Figs. 4.6 and 4.7 provide a comparison between the absolute backscattered spectra at $r = 50\ \mathrm{m}$, , $20\ \mathrm{cm}$, respectively, for rigid spheres with radii 5, 8 cm and 10, 15, $20\ \mathrm{cm}$, respectively. Fig. 4.8 demonstrates the effect of the variation of the material density of the sphere on the backscattered spectral amplitudes. The graph in Fig. 4.9 demonstrates the inverse relation between the spectral spacing ΔF (Hz) and the radius of a rigid and a non-rigid sphere for the purpose of extracting the sphere radius for metals that have $c_e = 3000\mathrm{m/s}$. We notice also in this graph that ΔF increases in the case of the non-rigid sphere, but not for the rigid sphere with the same radius. This results from the increase of the sound speed in the mild steel in comparison with the surrounding medium (water). We have plotted the absolute spectrum of the scattered fields and their corresponding time histories at distance $r = 150\ \mathrm{m}$ and $\theta_0 = 0, \pi/6, \pi/3, \pi/2, 2\pi/3,\ 5\pi/6, \pi$ for a rigid sphere with radius $a = 3,\ 4,\ 5\ \mathrm{cm}$ in Figs 4.11-4-22. These graphs show that the backscattered spectral amplitudes increase as the radius increases. Furthermore, the bandwidth of the spectra decreases in the forward directions as the radius increases. Consequently, the pulses have larger widths in the time domain. This is illustrated in Fig. 4.10, where a comparison is made of the time history of the backscattered pulses at

$r = 50$ m from rigid spheres with radii $a = 5$ and 8 cm. The delay between the spikes of the pulses is clearly evident.

4.9 Extraction of the Radius from the Backscattered Spectrum

We have successfully investigated the relation between the spectral spacing ΔF and the radius of the sphere as a guide for extracting the radius from the backscattered spectrum. For most metals the parameter c_e (speed of sound) is approximately 3000m/s [147]. This helps in obtaining excellent estimates of the radius of the scatterer from the graphs shown in Fig. 4.9. The relative error depends mainly on the difference between c_e of the sphere and 3000m/s. We have provided two graphs for this estimation. The first one, for a rigid sphere, shows that the backscattered spectrum is independent of the material parameters. The second graph is for a sphere made of mild steel as an actual scatterer. Following this procedure, we have estimated the radii for spherical scatterers made from different materials at specific observation distances. The results are summarized in Table 4-I.

4.10 Conclusions

We have examined the scattering of a MPS pulse from soft and rigid spheres. This work has important applications in many physical areas. We have discussed the effect of the variation of material parameters on the amplitude spectrum of such ultra-wideband pulses in the acoustic range $f\,(1\text{ KHz} \rightarrow 150\text{ KHz})$. The analysis allows the extraction of the radius of the sphere from the backscattered spectrum for different metals [cf. Table 4.1]. The error of the estimation is greater in the case of a cast iron sphere (6%) than a Nickel sphere due to the relatively large difference between the two values of c_e. In view of the time history of the scattered pulse, we can see clearly the difference in the value of the pulse width $(\approx 20\mu s)$ of the exact MPS pulse and the backscattered one $(\approx 12\mu s)$, which

shows a decrease in the energy of the scattered pulse. This decrease is attributed to the spreading in all directions. Therefore, part of the scattered power returns back into the source. Such a backscattered pulse is considered as a modulating signal because it contains the effects of the physical parameters (size of the sphere) and the material constituting the sphere. It is preferable to extract the information about the size from the first region of the spectrum. This is ascribed to the more accurate values resulting from the computation of the exact series solution for small arguments with respect to the order of the spherical functions given in Eq. (4.7.3). A distinct feature related to the type of the material is indicated in the graphs for a non-rigid sphere, which obviously show that we can extract information about this type from the backscattered spectrum. The results in our work have been obtained for a sphere immersed in water with density $\rho = 10^3 \text{kg} / \text{m}^3$ and speed $c = 1500 \text{ m} / \text{s}$, which is different from the speed of the acoustic wave inside the scatterer (sphere). The absolute scattered pressure spectrum in the forward directions $\left(\theta_0 = 0, \pi/6, \pi/3\right)$ is larger than that in the backward directions $\left(\theta_0 = \pi/2, 2\pi/3, 5\pi/6, \pi\right)$. This is due to the constructive interference between the creeping waves and the direct waves, especially for spheres with radii close to the waist of the incident pulse. In general this gives rise to wider bandwidths and, subsequently, to shorter pulse lengths in the forward directions. The spectral spacing in the backward directions decreases as the radius increases. In addition, the peaks become more obvious in such directions, in a way that enables one to easily extract the radius of the sphere. As we might expect, a distortion starts to appear in the scattered forward pulses as the radius of the sphere becomes larger than the waist of the pulse. This arises because of the diffraction of the incident acoustic pressure by the spheres. The scattered waveform in the time domain consists of an initial spike that can be predicted by geometrical optics. This spike is followed by another peak, corresponding to the incident pulse traveling around the surface of the sphere (creeping wave) in the manner predicted by the geometrical theory of diffraction. Such a later peak

appears with a delay directly proportional to the radius of the sphere $\left(2\pi a/c = 0.125 \text{ ms}\right)$ for $a = 3 \text{ cm}$.

The results presented in this chapter are very encouraging because they show a real potential to deduce the physical attributes of the scattering sphere from the scattered field. A future objective is to change the surrounding medium in order to see its effect on the spectrum. Another interesting objective is to control the parameters of the MPS pulse in order to extend its frequency band and adapt the analysis for electromagnetic problems. Finally, it is worthwhile mentioning that the scattering of LW pulses still needs more work in order to investigate the effects of the different media and to enhance the return signal from targets with complicated shapes.

Sphere Material	Actual Radius (cm)	Spectral Spacing (ΔF) in (KHz)	c_e value (m/s)	Distance from the source (cm)	Estimated Radius (cm)	Percent Error
Stainless Steel	6	4.894	3100	30	5.8	3.3
Stainless Steel	5	5.69	3100	20	4.9	2.0
Aluminum	4	7.429	3040	25	4.2	5.0
Aluminum	3	10.008	3040	35	2.9	3.0
Cast iron	5	5.689	2809	20	5.3	6.0

Table 4.1: Sphere radii extracted from the backscattered spectra

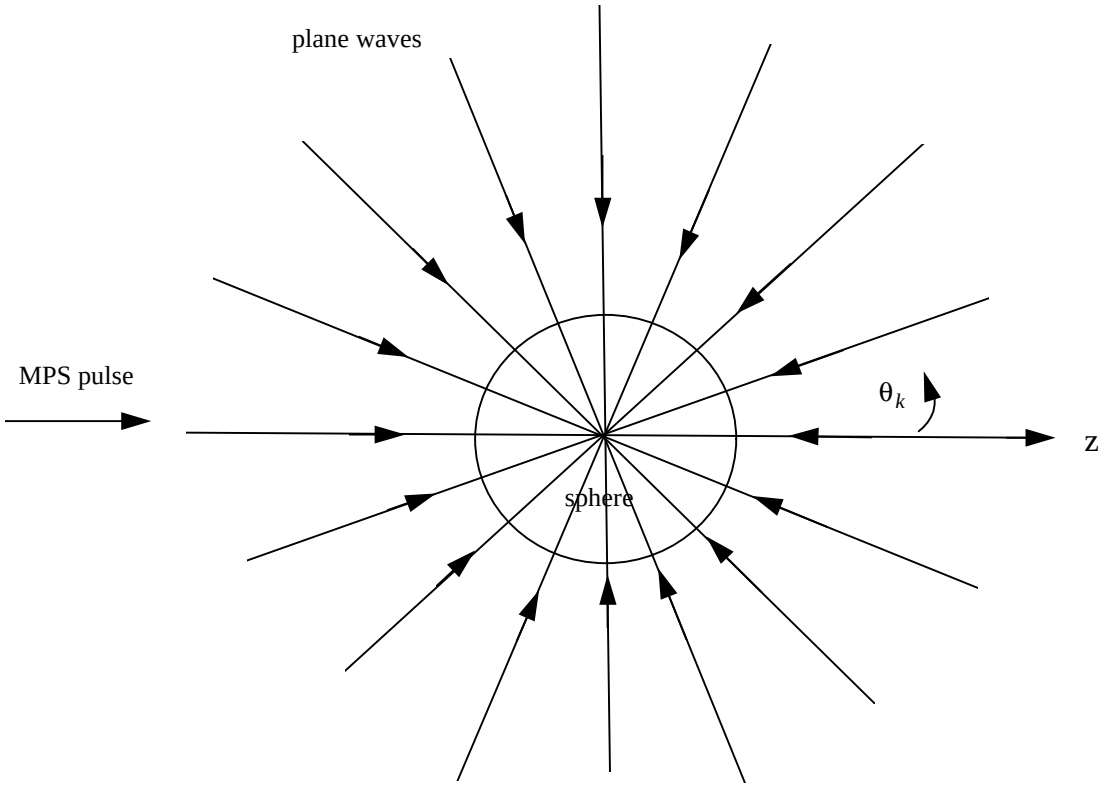

Figure 4.1: The equivalence between weighted plane waves incident on the sphere from different directions and the MPS pulse.

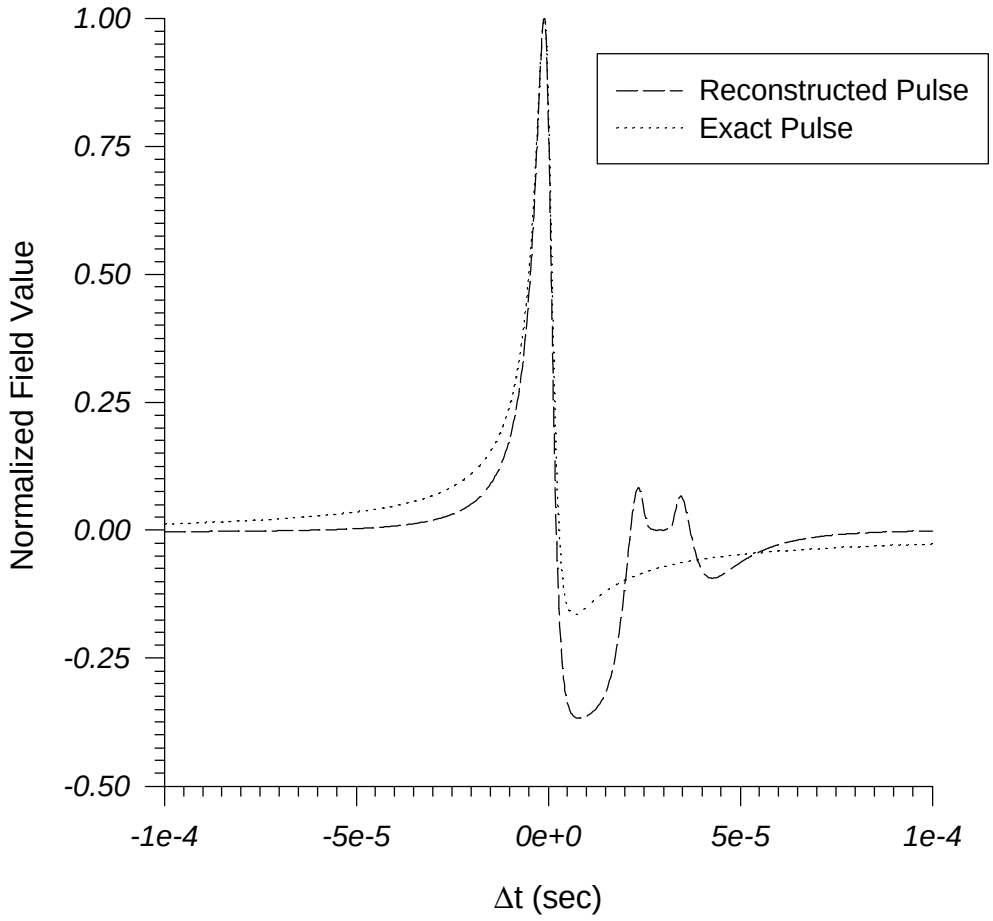

Figure 4.2: A comparison of the time histories of the exact and the reconstructed MPS pulses at $r = 15\,\text{cm}$.

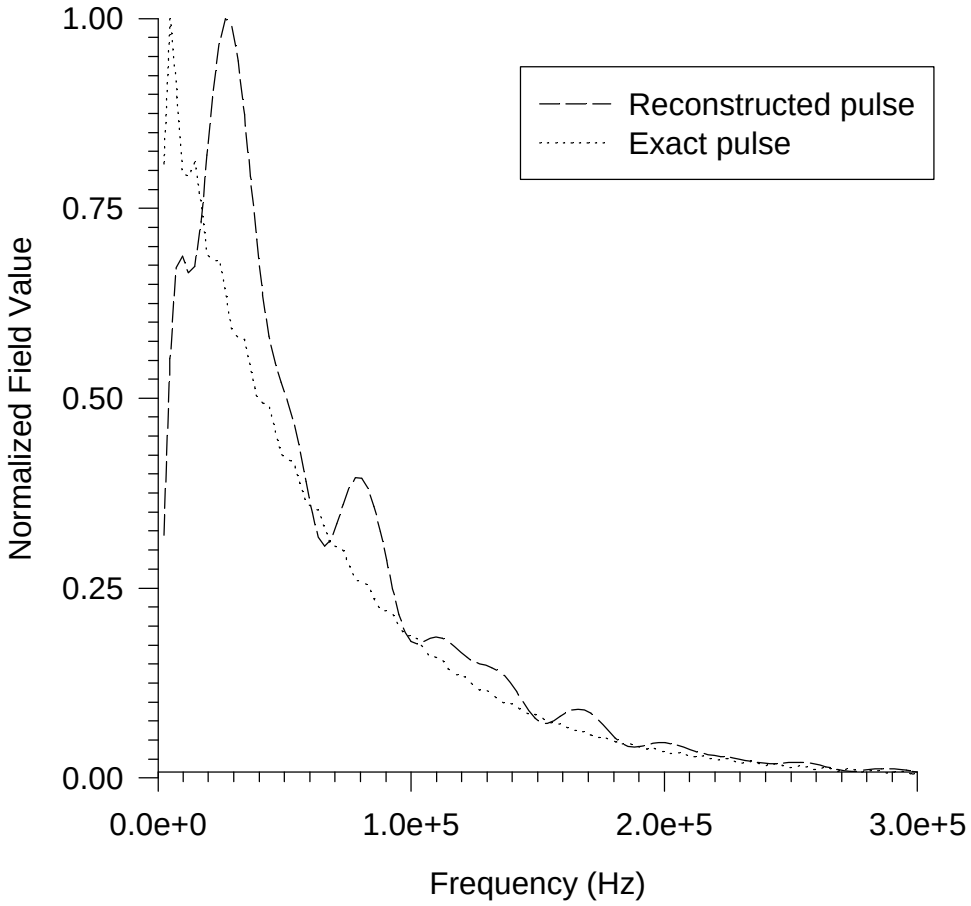

Figure 4.3: Fast Fourier transform of the time history related to the exact incident and reconstructed pulses in Fig. (4.2).

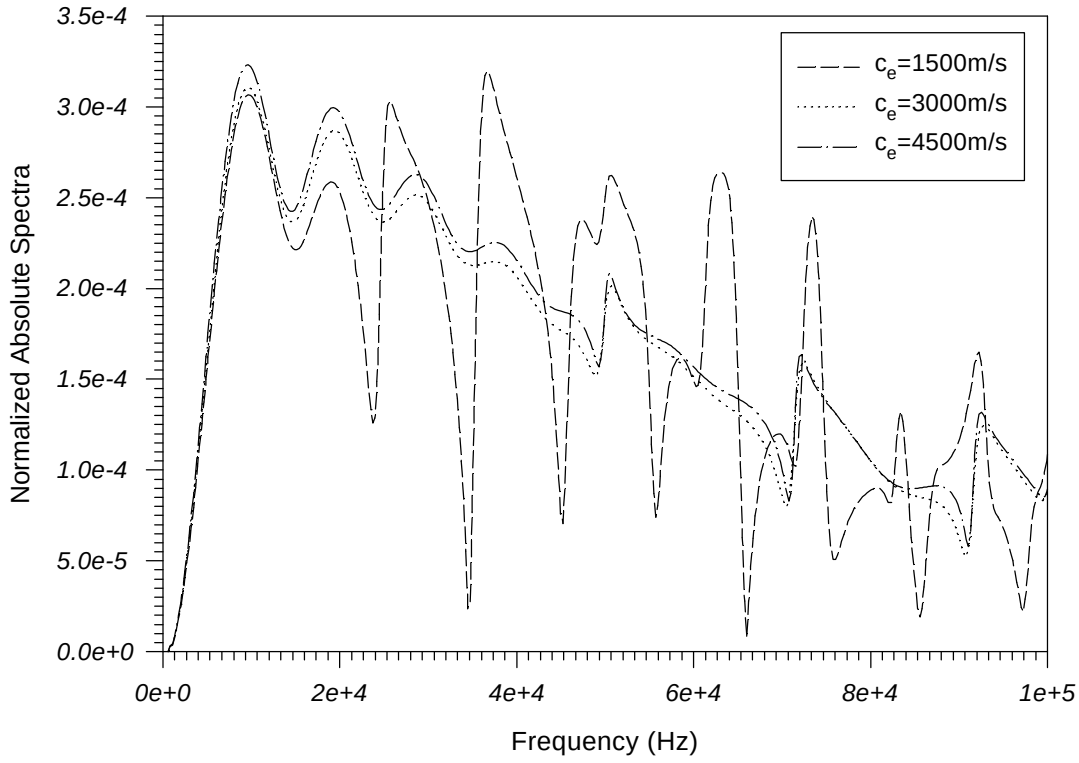

Figure 4.4: Predicted backscattered spectrum of the MPS pulse from a sphere with $\rho_e = 7.8 \times 10^3 \text{kg/m}^3$, $a = 30\text{mm}$ and different speeds c_e. The observation distance r equals 15 cm.

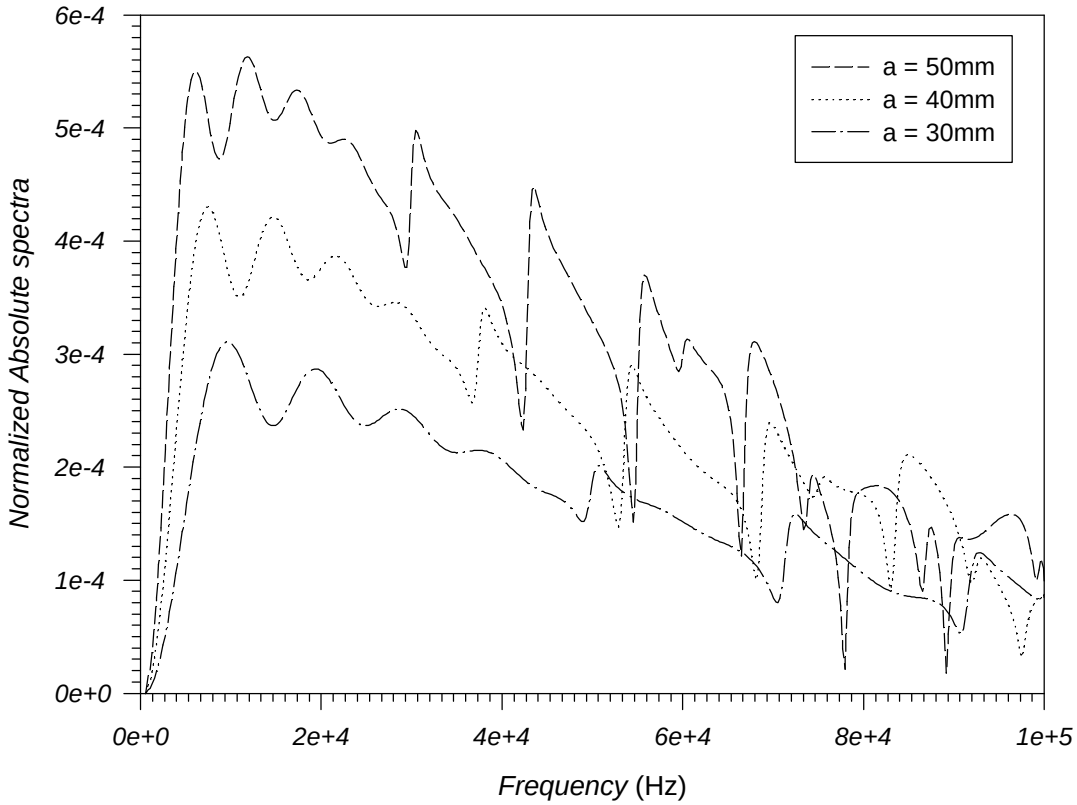

Figure 4.5: Predicted backattered spectrum of the MPS pulse from a sphere with $c_e = 3000\text{m/s}$, $\rho_e = 7.8\times10^3\text{kg/m}^3$ and different radii. The distance from the sphere is 15 cm.

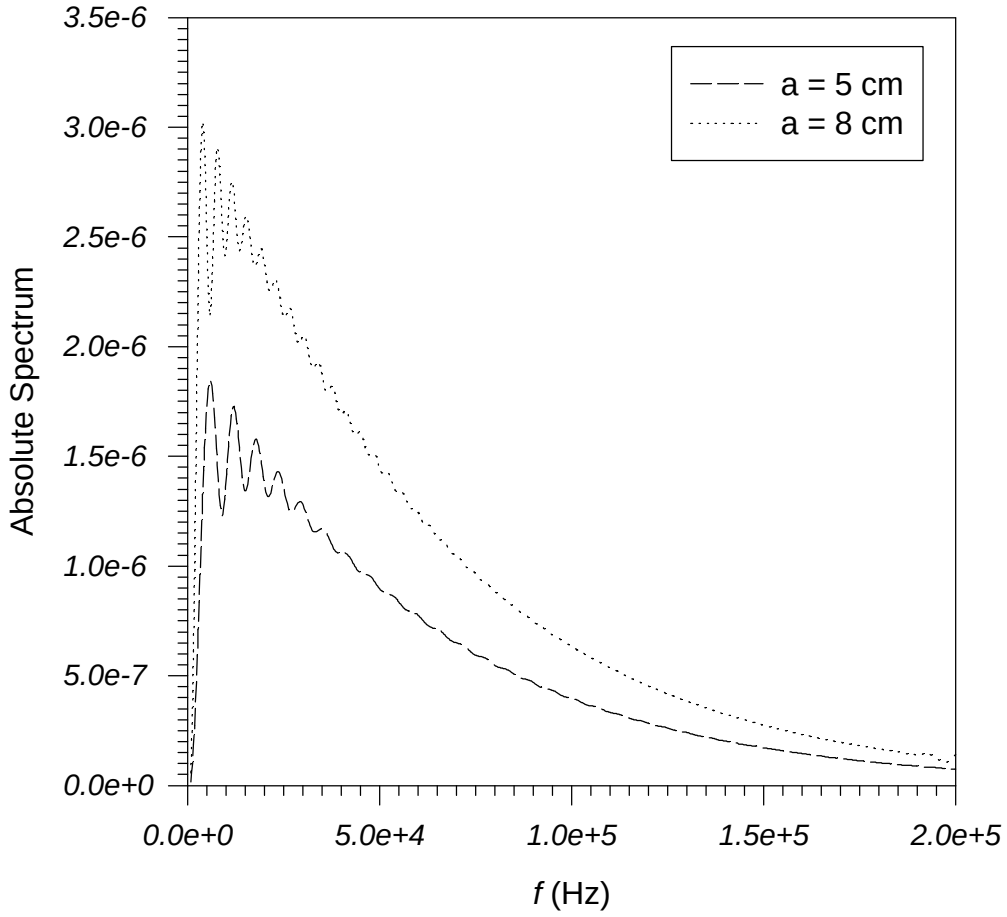

Figure 4.6: The backscattered spectra at $r = 50$ m from a hard sphere with radius $a = 5$ and 8 cm.

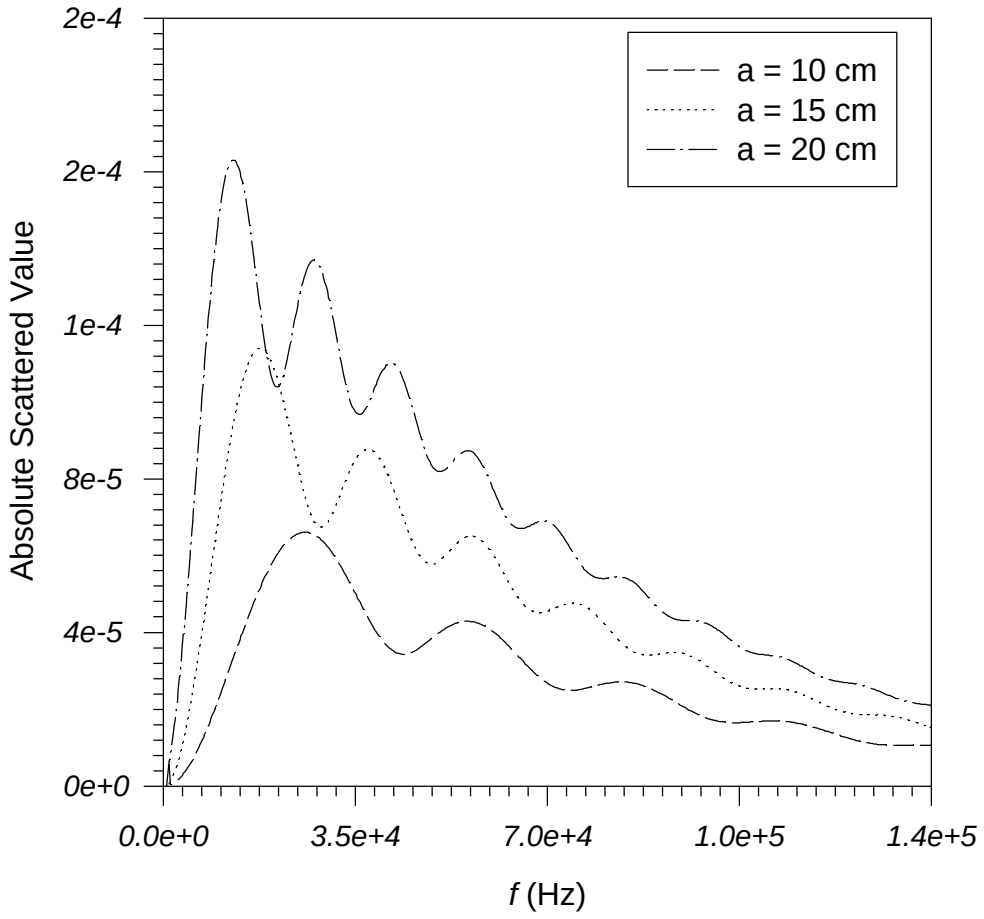

Figure 4.7: The backscattered spectra at $r = 20$ cm from a hard sphere with radius 10, 15 and 20 cm.

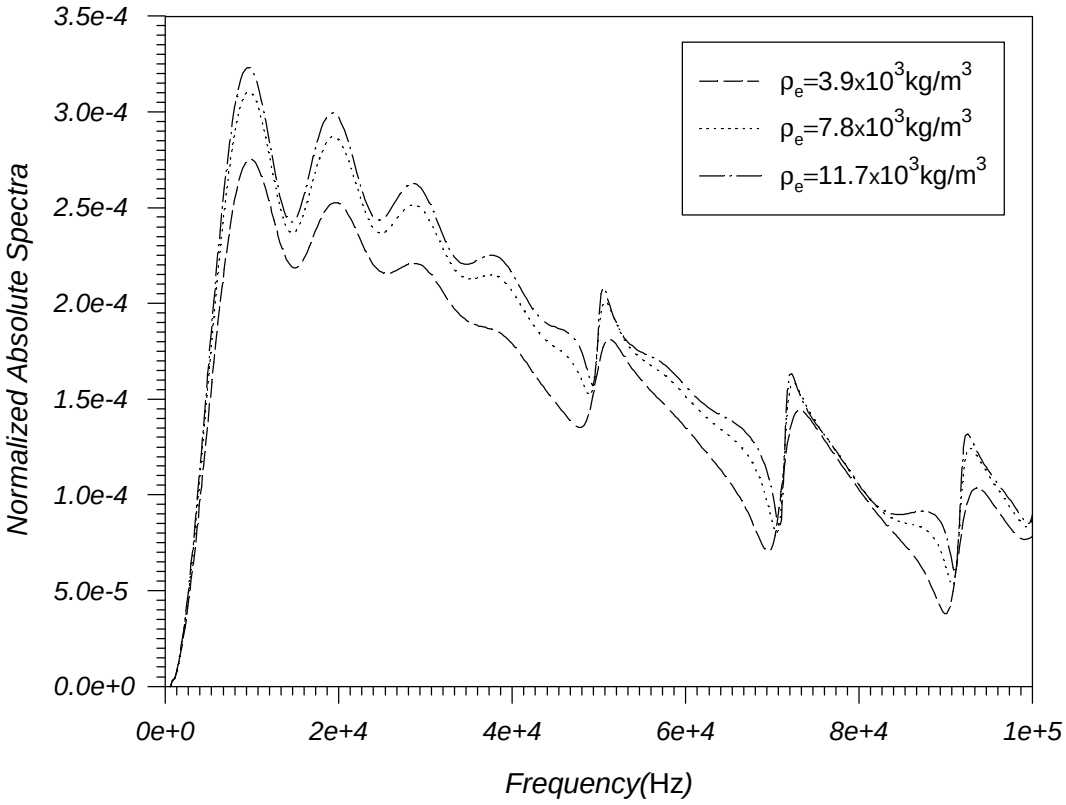

Figure 4.8: Backscattered spectra from a sphere with $a = 30\text{mm}$, $c_e = 3000\text{m/s}$ and different material densities ρ_e. The distance from the sphere is 15 cm.

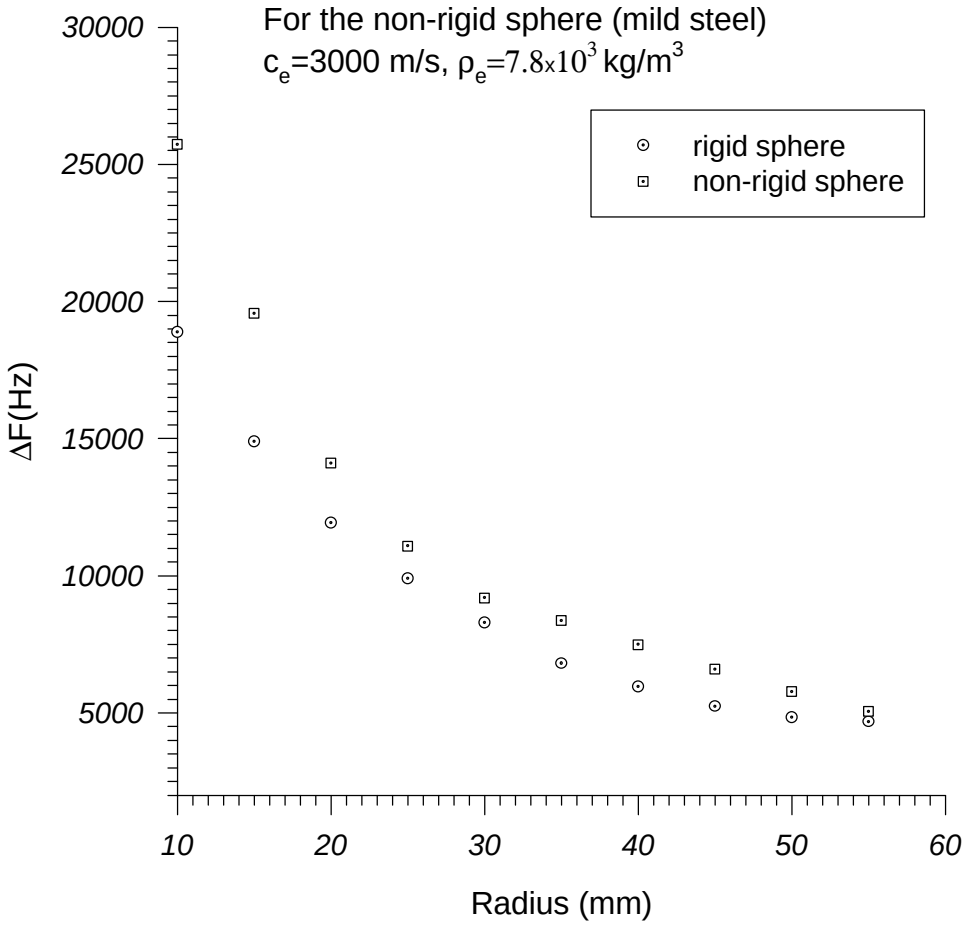

Figure 4.9: The variation of the sphere radius and the spectral spacing between two adjacent peaks of the backscattered spectrum of a rigid and a non-rigid sphere at r = 15cm. The sphere is immersed in water for both cases.

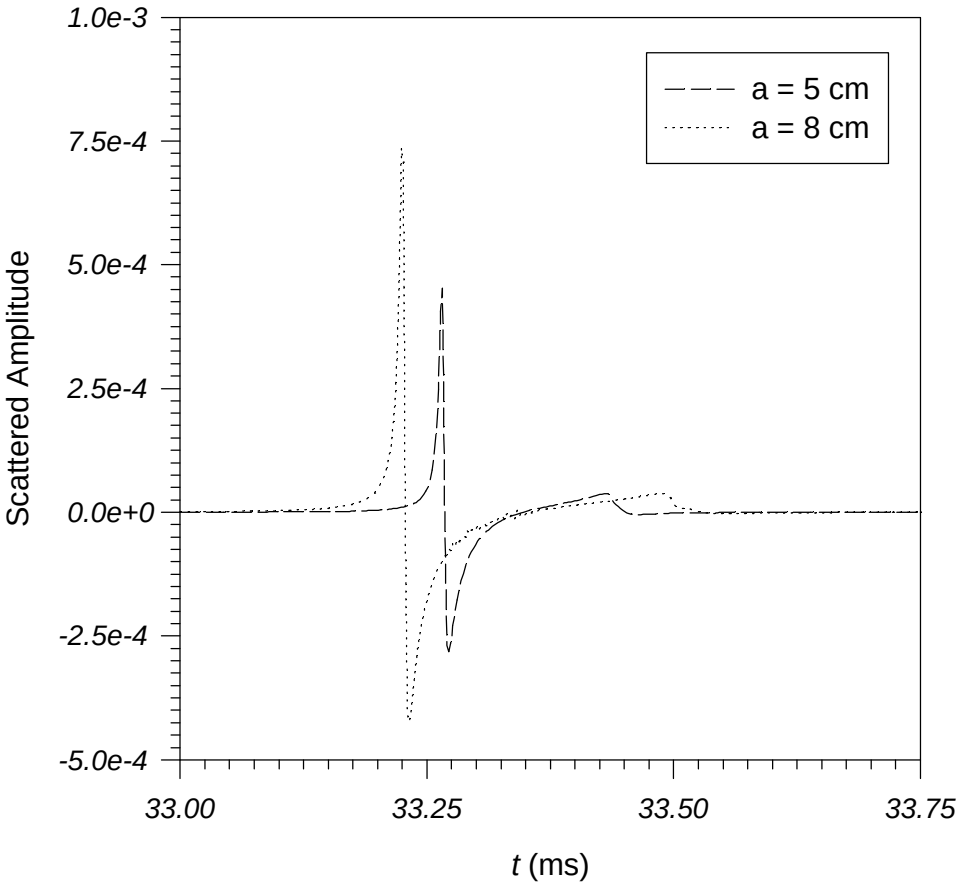

Figure 4.10: Time history of the backscattered MPS pulse at $r = 50$ m from a hard sphere with radii $a = 5$ and 8 cm. We notice that the delay between the two peaks for the sphere with radius $a = 8$ cm is larger than that with radius $a = 5$ cm.

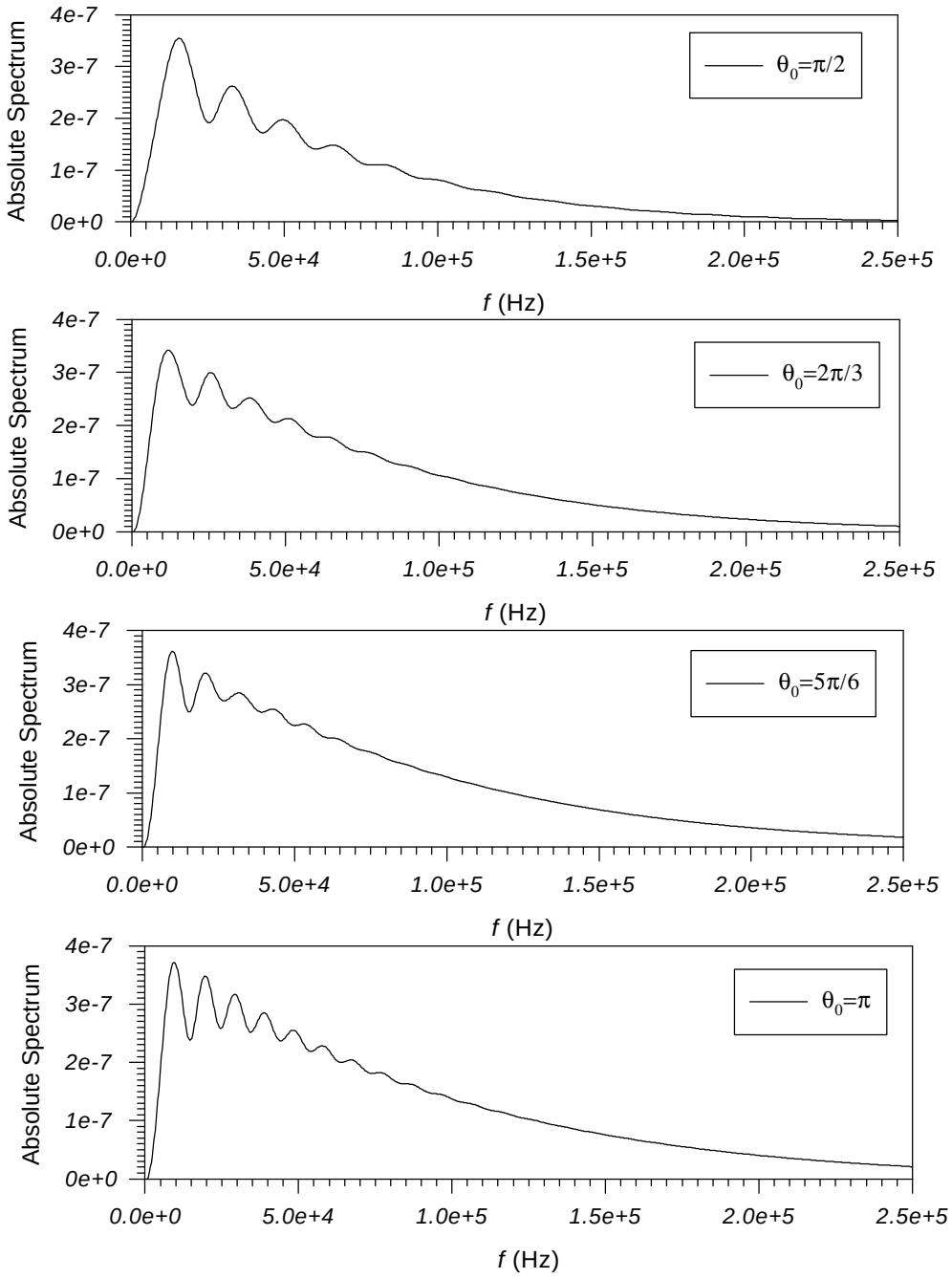

Figure 4.11: Bistatic scattered spectra at $r = 150$ m, $\theta_0 = \pi/2,\ 2\pi/3,\ 5\pi/6$ and π of the MPS pulse from a rigid sphere with radius $a = 3$ cm immersed in water.

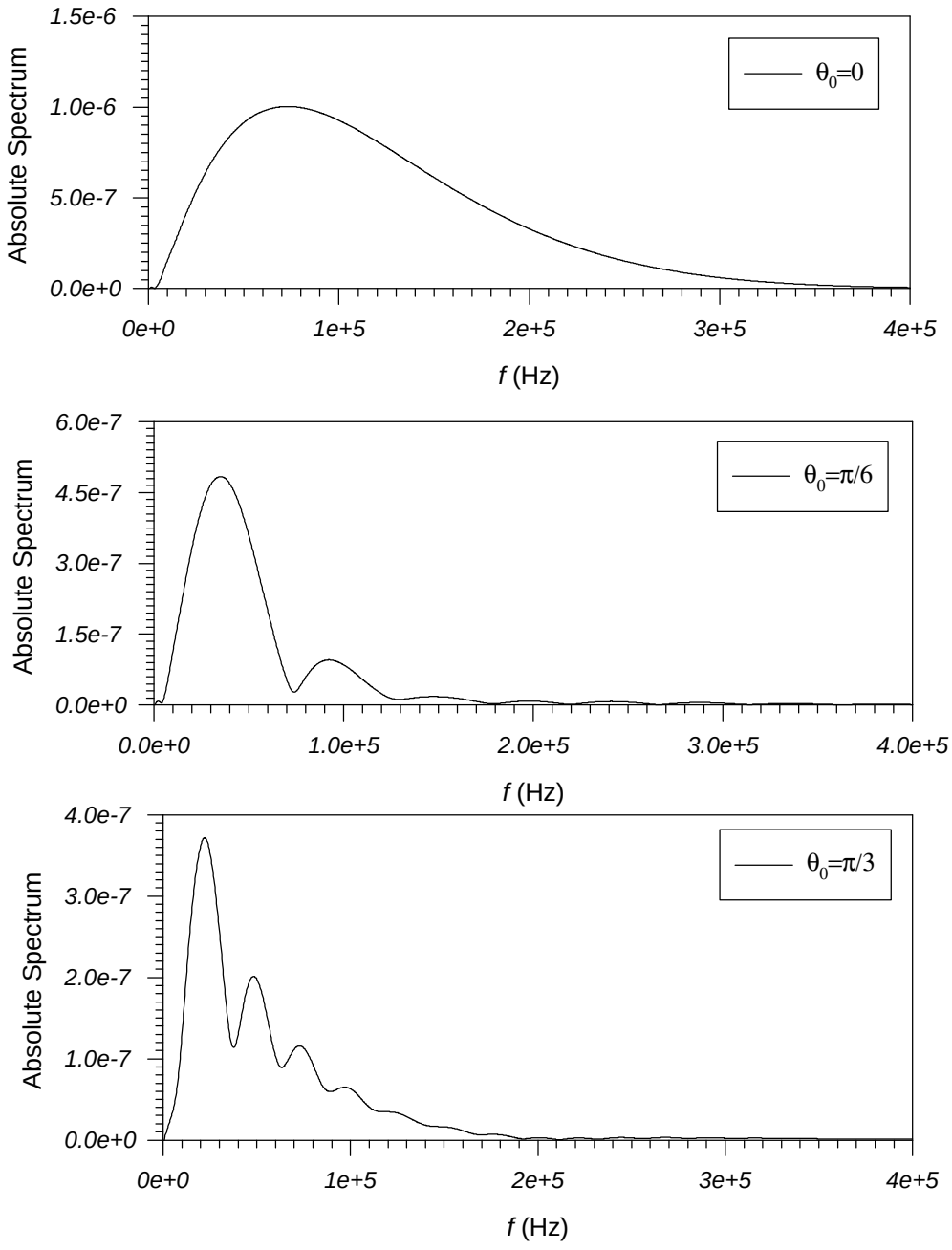

Figure 4.12: Bistatic scattered spectra at $r = 150$ m, $\theta_0 = 0,\ \pi/6$ and $\pi/3$ of the MPS pulse from a rigid sphere with radius $a = 3$ cm immersed in water.

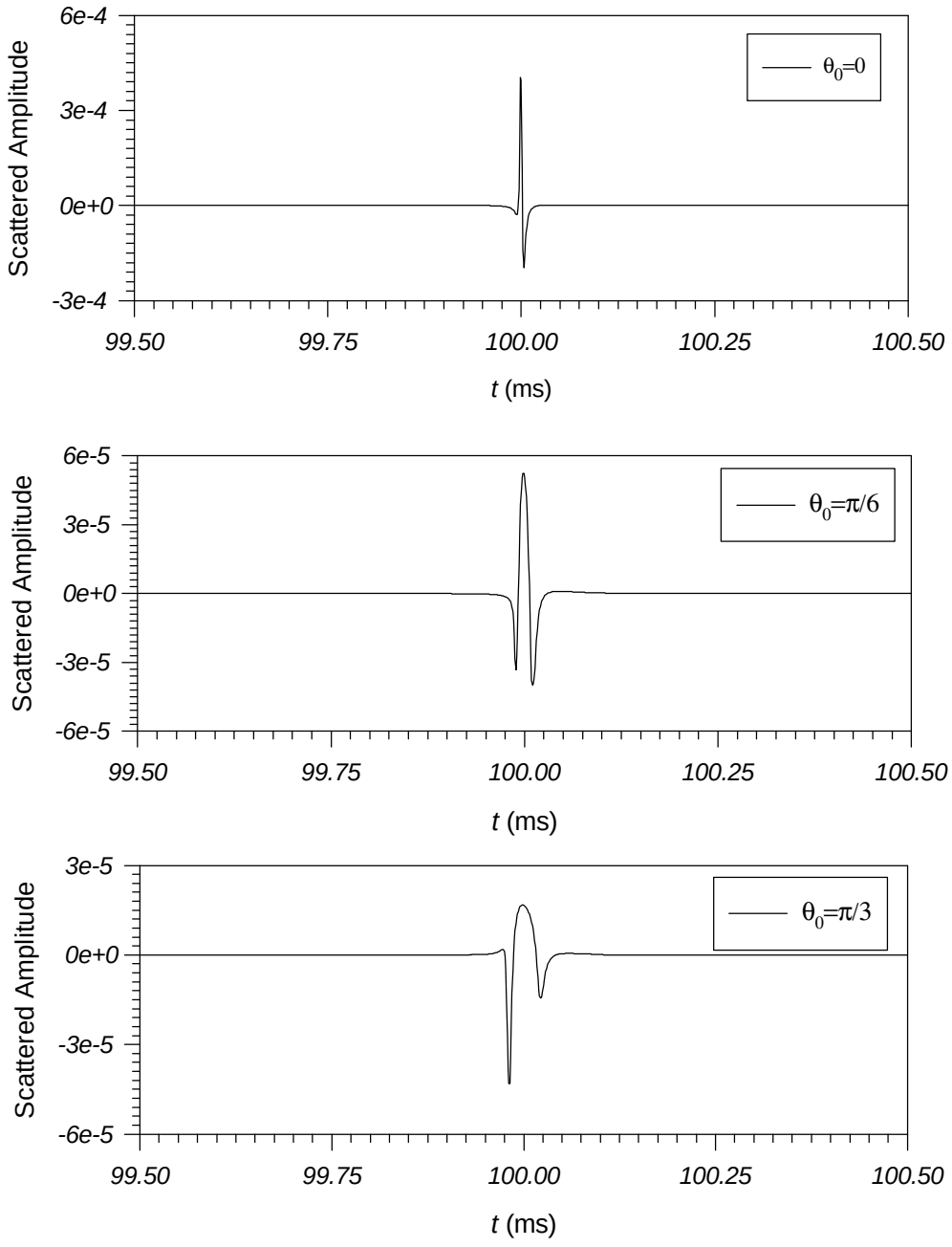

Figure 4.13: Time history of the scattered MPS pulse at $r = 150$ m, $\theta_0 = 0, \pi/6$ and $\pi/3$ from a rigid sphere with radius $a = 3$ cm immersed in water.

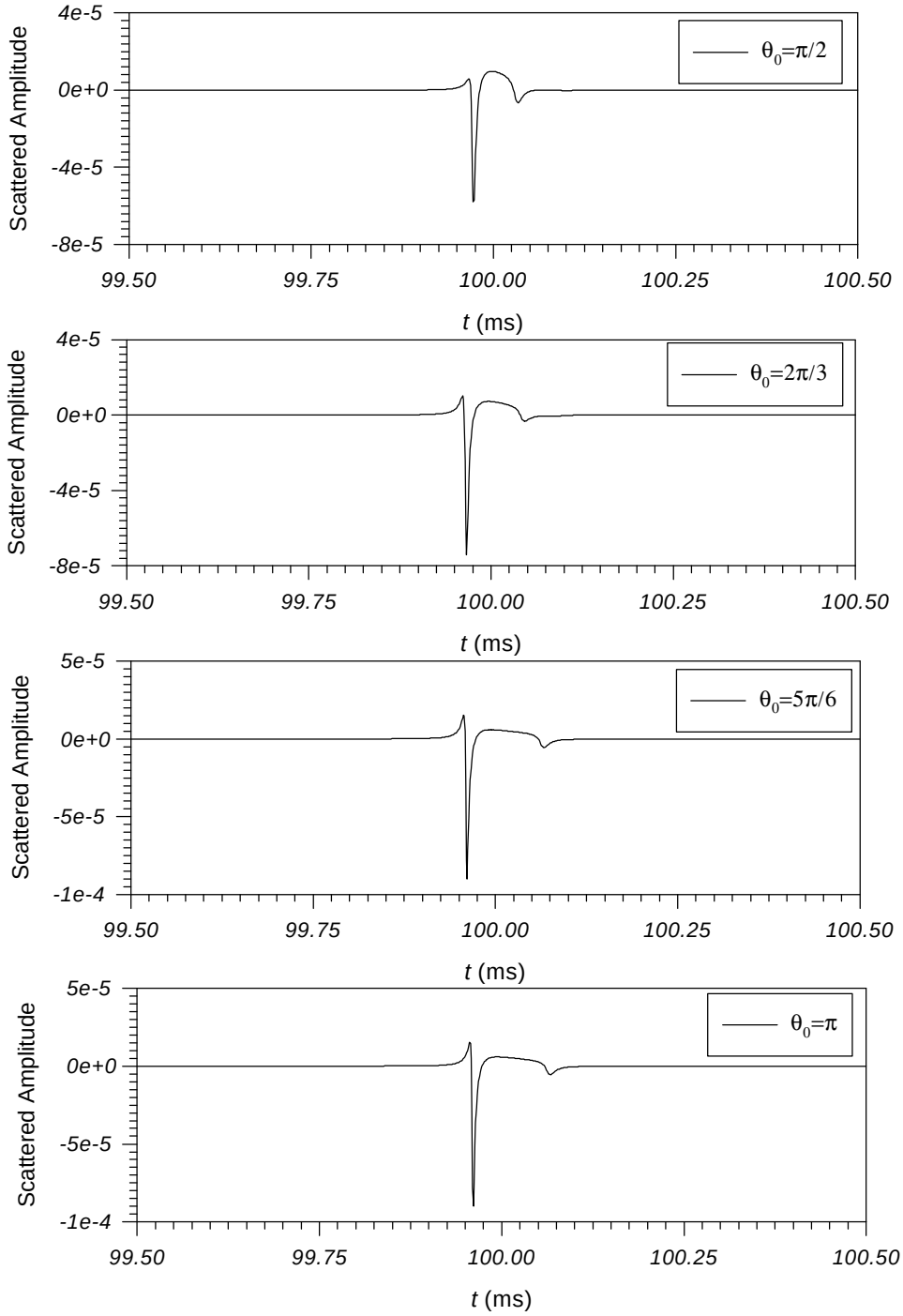

Figure 4.14: Time history of the scattered MPS pulse at $r = 150\text{m}$, $\theta_0 = \pi/2,\ 2\pi/3,\ 5\pi/6$ and π from a rigid sphere with radius $a = 3\text{ cm}$ immersed in water.

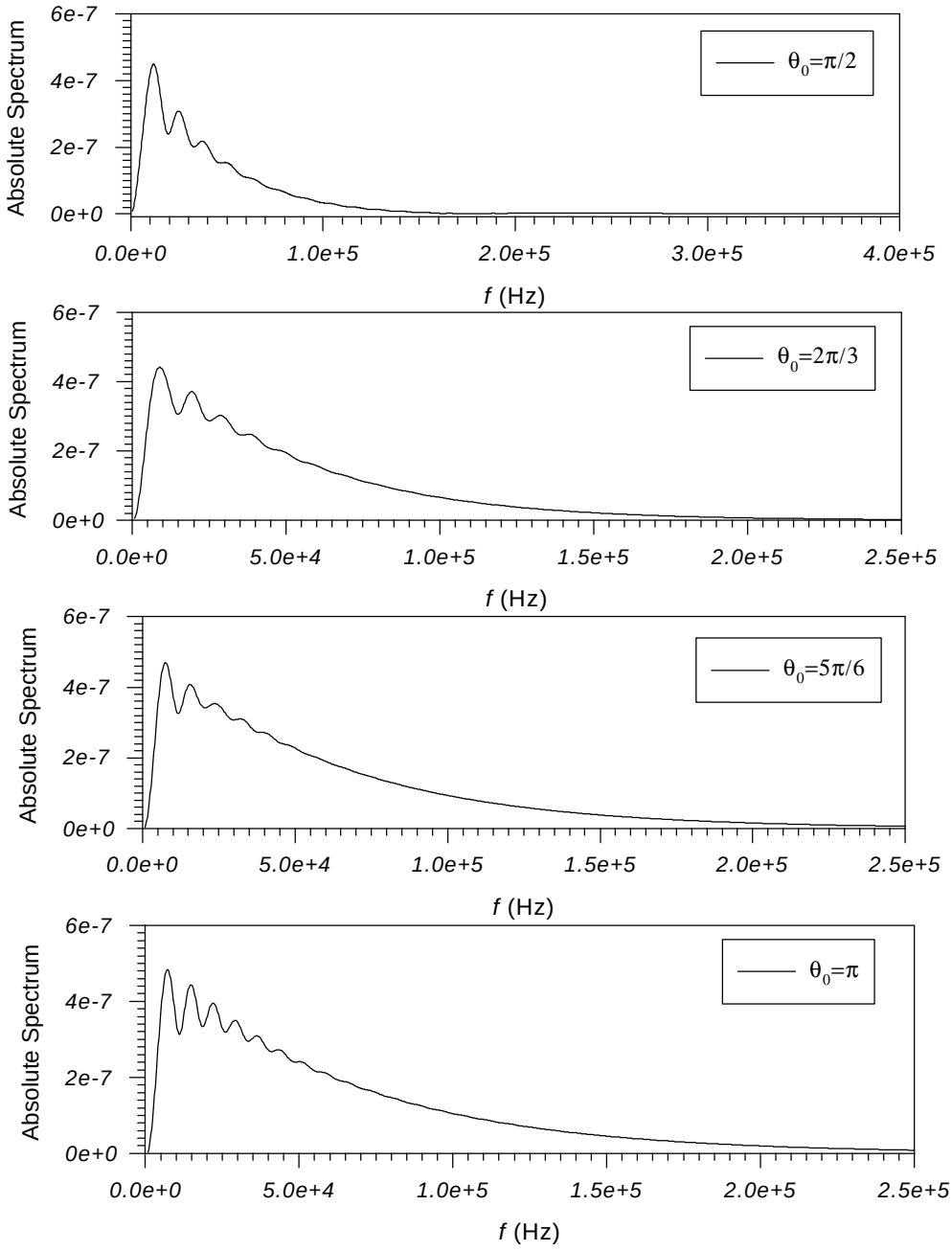

Figure 4.15: Bistatic scattered spectra at $r = 150$ m, $\theta_0 = \pi/2,\ 2\pi/3,\ 5\pi/6$ and π of the MPS pulse from a rigid sphere with radius $a = 4$ cm immersed in water.

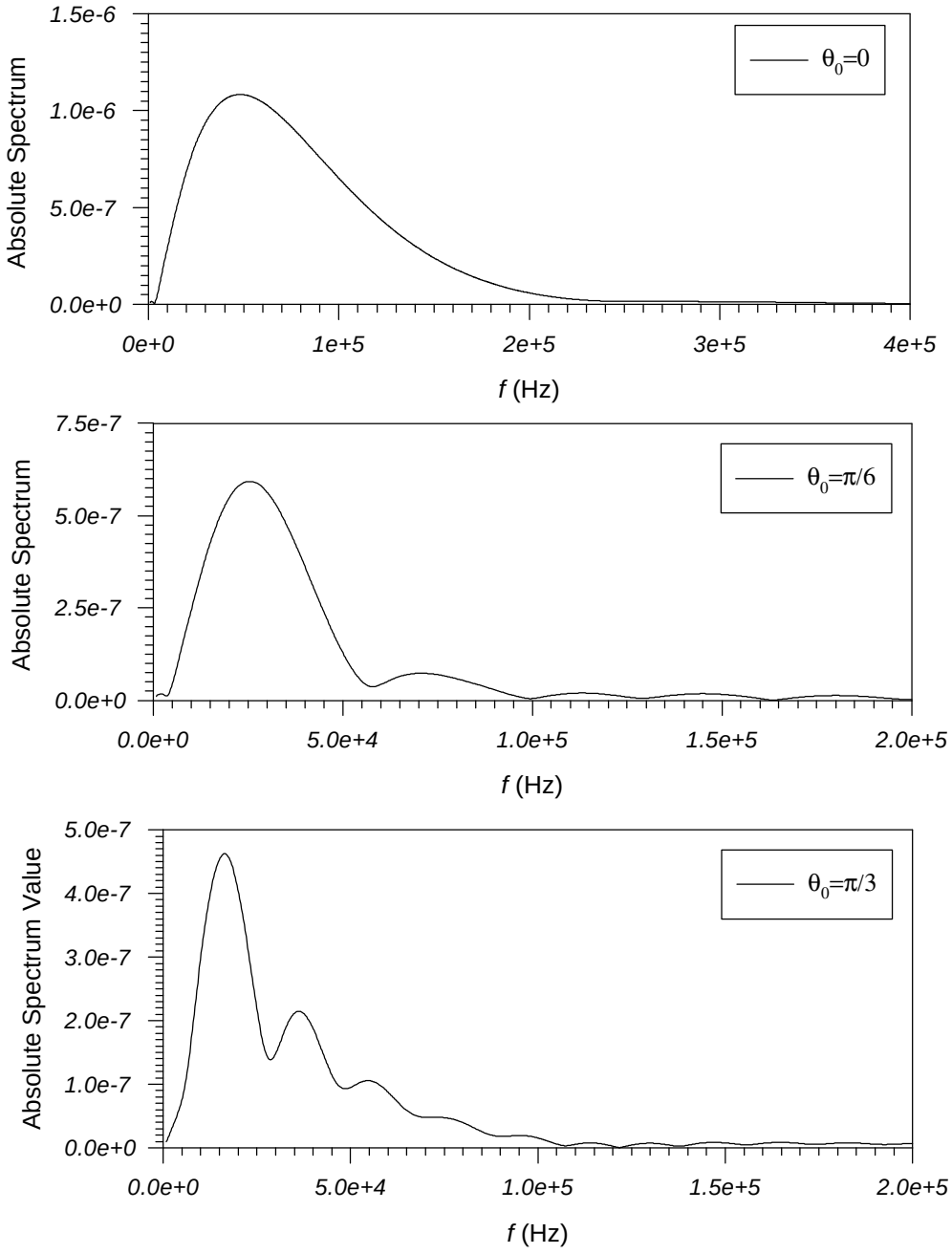

Figure 4.16: Bistatic scattered spectra at $r = 150$ m, $\theta_0 = 0,\ \pi/6$ and $\pi/3$ of the MPS pulse from a rigid sphere with radius $a = 4$ cm immersed in water.

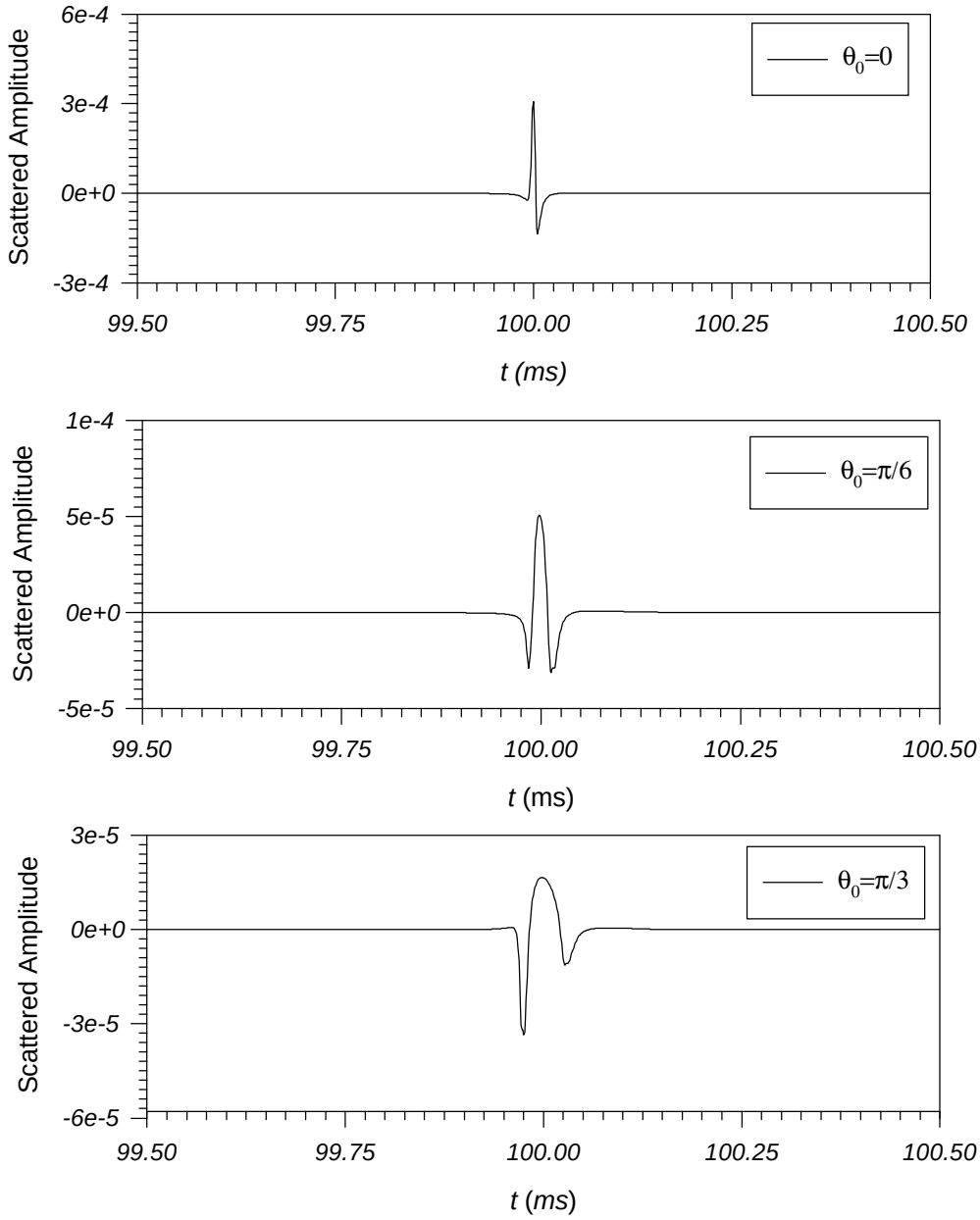

Figure 4.17: Time history of the scattered MPS pulse at $r = 150$ m, $\theta_0 = 0, \pi/6$ and $\pi/3$ from a rigid sphere with radius $a = 4$ cm immersed in water.

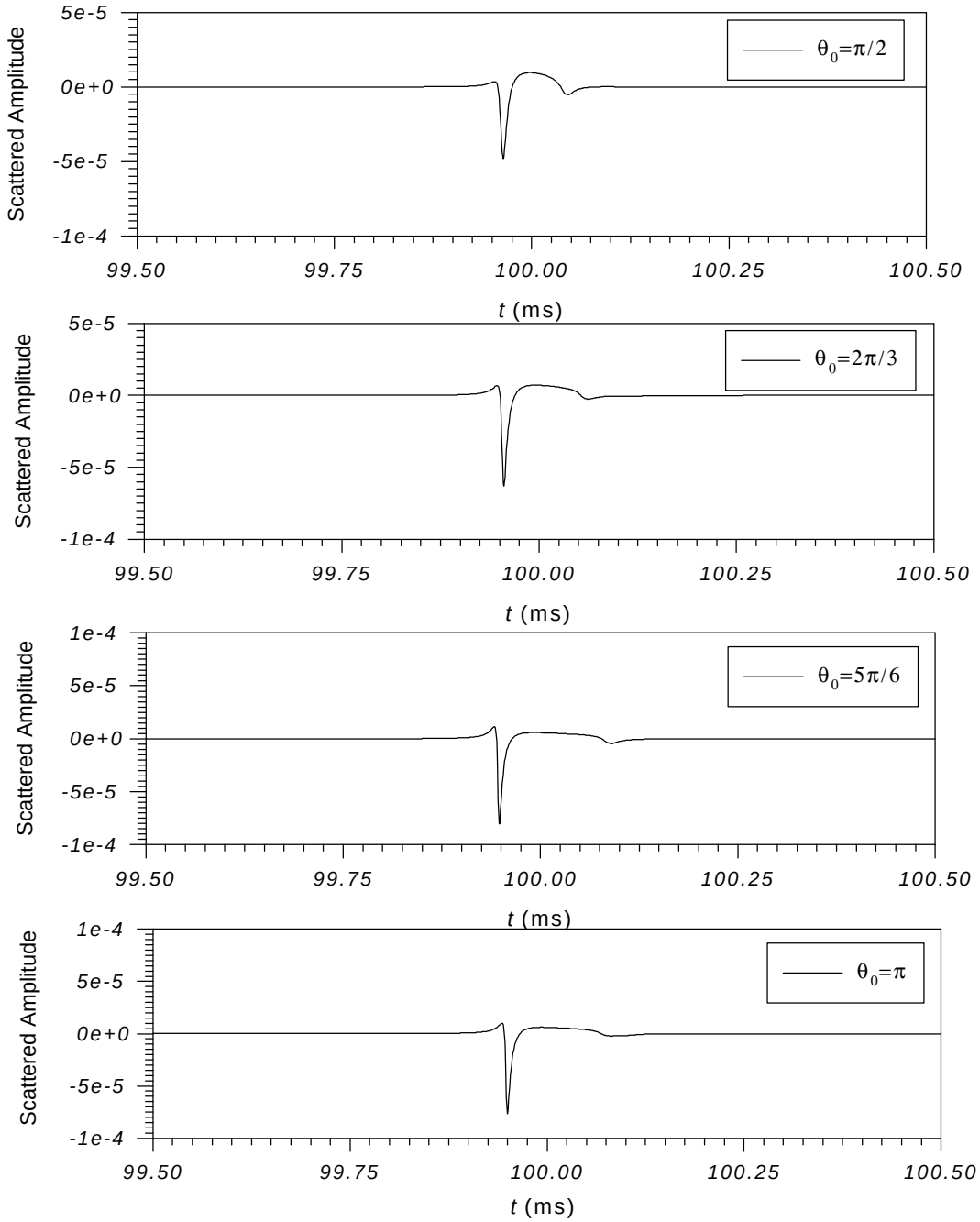

Figure 4.18: Time history of the scattered MPS pulse at $r = 150$ m, $\theta_0 = \pi/2,\ 2\pi/3,\ 5\pi/6$ and π from a rigid sphere with radius $a = 4$ cm immersed in water.

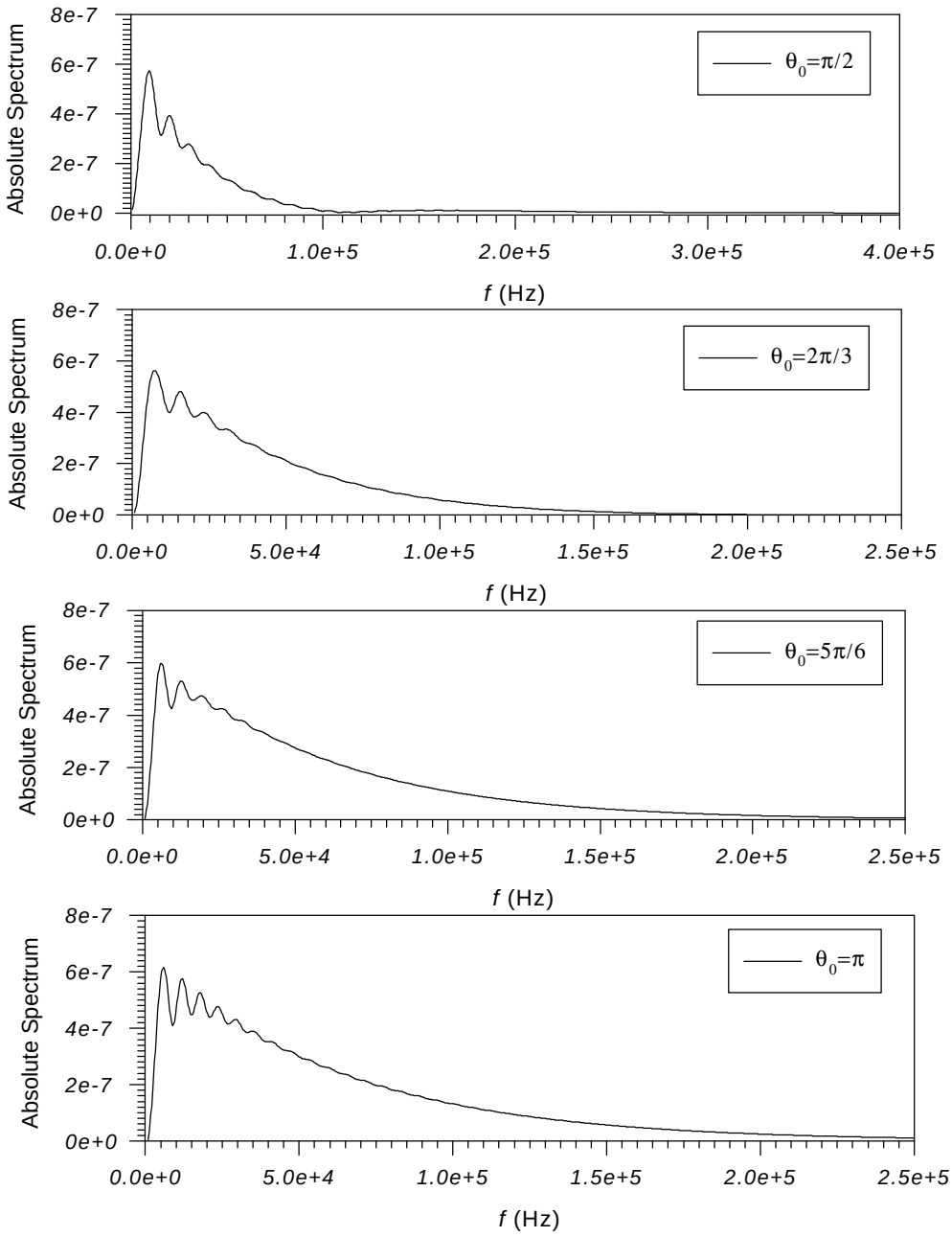

Figure 4.19: Bistatic scattered spectra at $r = 150$ m, $\theta_0 = \pi/2,\ 2\pi/3,\ 5\pi/6$ and π of the MPS pulse from a rigid sphere with radius $a = 5$ cm immersed in water.

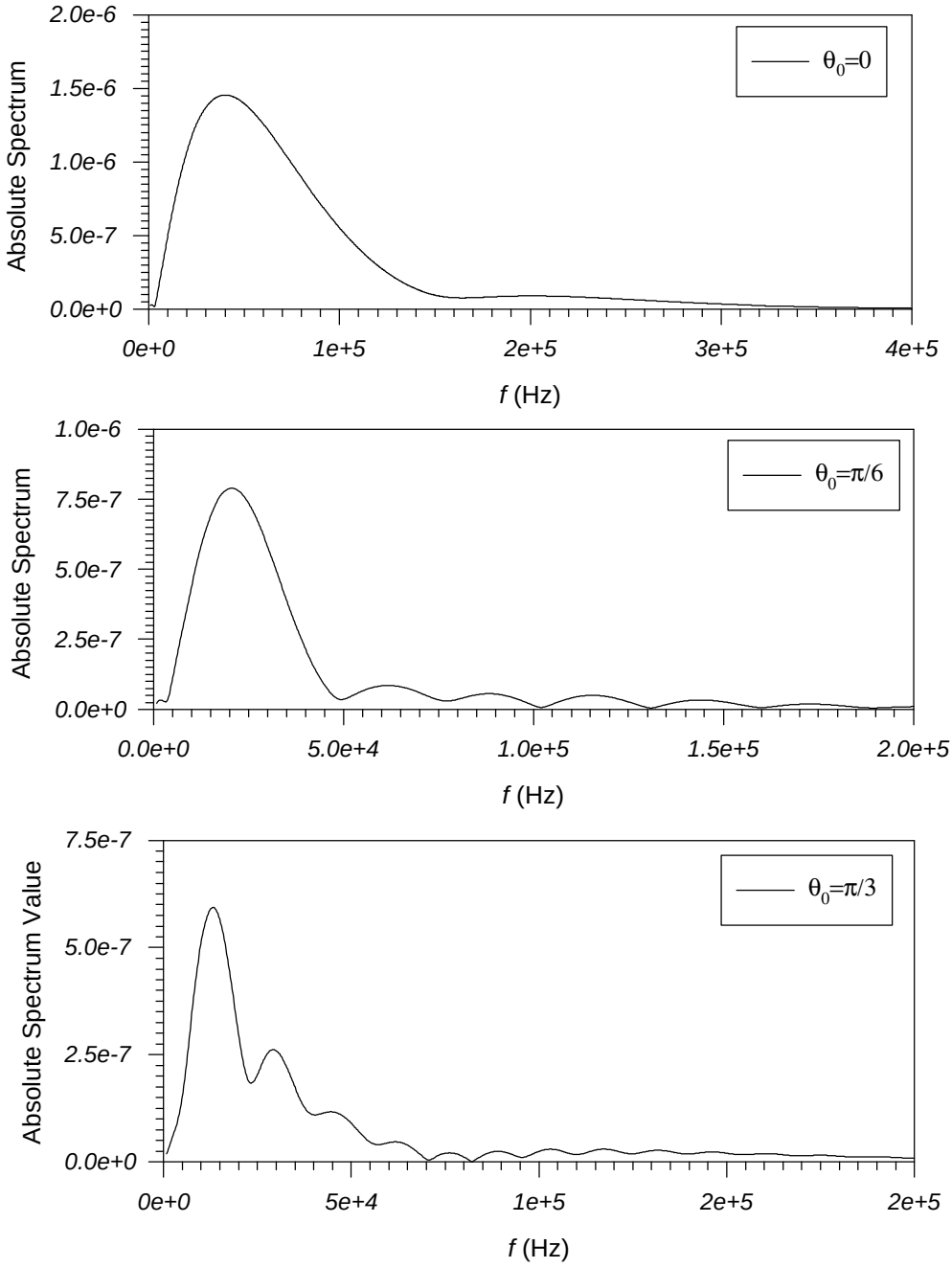

Figure 4.20: Bistatic scattered spectra at $r = 150$ m, $\theta_0 = 0,\ \pi/6$ and $\pi/3$ of the MPS pulse from a rigid sphere with radius $a = 5$ cm immersed in water.

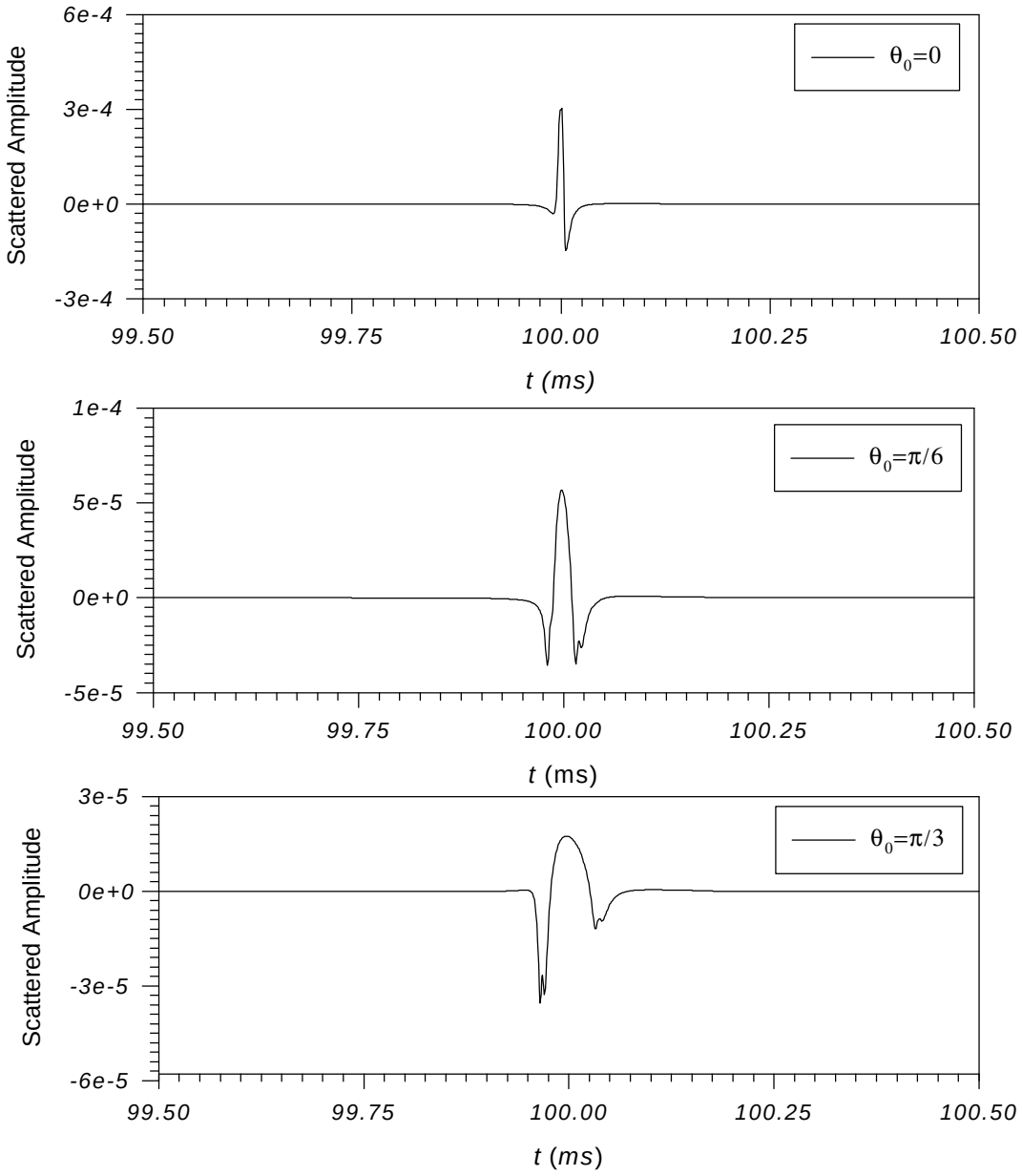

Figure 4.21:Time history of the scattered MPS pulse at $r = 150$ m, $\theta_0 = 0, \pi/6$ and $\pi/3$ from a rigid sphere with radius $a = 5$ cm immersed in water.

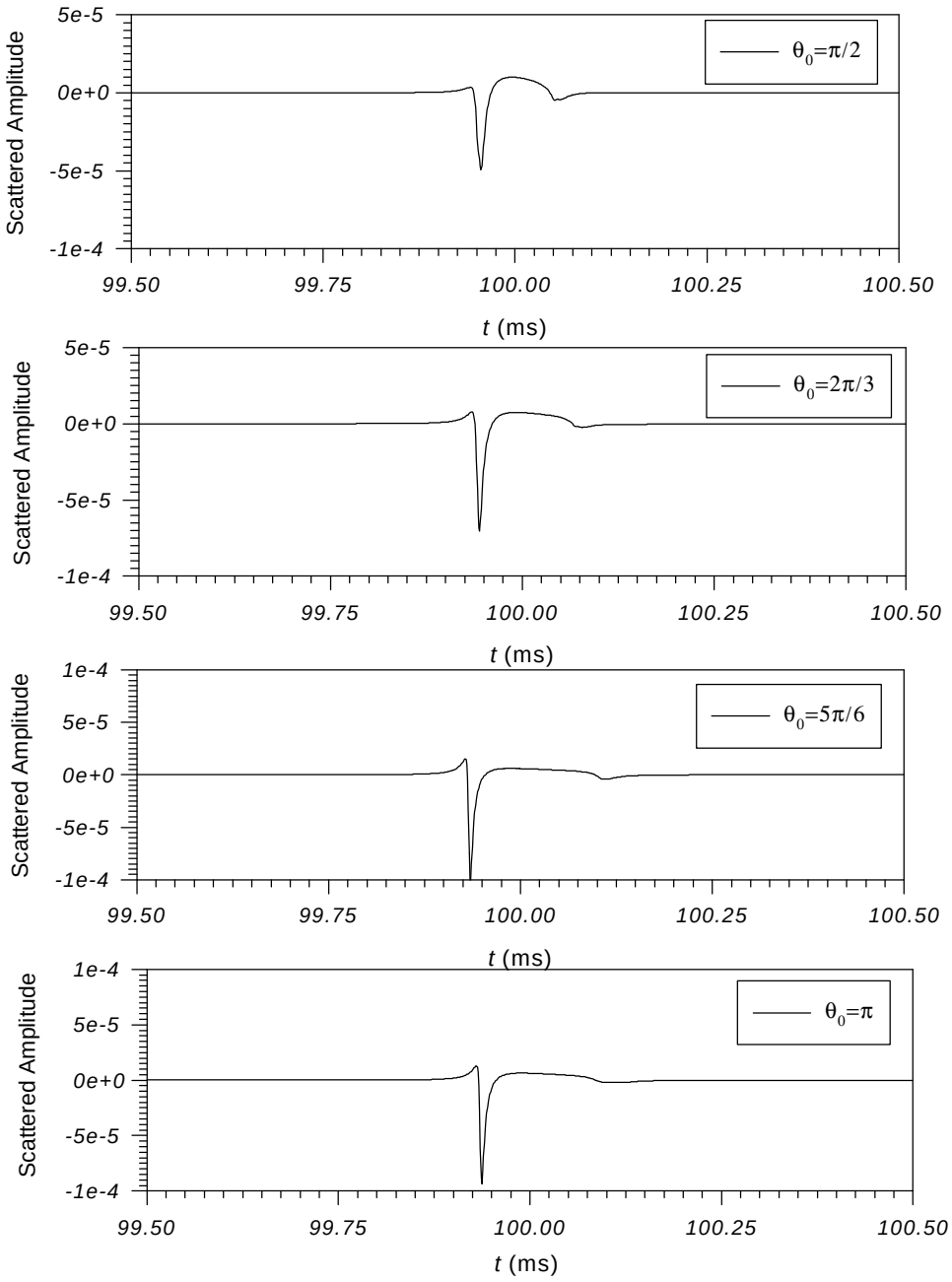

Figure 4.22: Time history of the scattered MPS pulse at $r = 150$ m, $\theta_0 = \pi/2,\ 2\pi/3,\ 5\pi/6$ and π from a rigid sphere with radius $a = 5$ cm immersed in water.